

A Spectral Journey Spectroscopy Report

Siddhant Pujni
s2344216

Four experiments are considered to explore foundational techniques in astronomical spectroscopy: Grating Spectrograph, Solar Spectrum, Prism Spectrometer, and Spectral lamps and Transmission Curves. Groove spacings of 900(12) nm and 1550(26) nm were determined, confirming the relationship between groove density and spectral resolution. Analysis of the Solar spectrum revealed Fraunhofer and telluric lines, highlighting the dependence of atmospheric absorption features on elevation. Measurements of the refractive index of a glass prism demonstrated its dependence on wavelength, with measurements aligning well with the Cauchy dispersion relation. Analysis of emission spectra from various gas lamps identified their composition as noble gases, while transmission curves generated using colour filters demonstrated their effectiveness in isolating specific spectral features.

I. INTRODUCTION

Astronomical observations are central to understanding the cosmos and constructing theoretical models that dictate the universe. This in turn has enabled numerous milestones, such as sending astronauts to the Moon, and holds promise for future endeavours such as human exploration of Mars. Observations in astronomy are made predominantly by studying electromagnetic radiation emitted by celestial objects [1]. However, conducting these observations introduces challenges such as cosmic variance, atmospheric interference, and the expenses associated with sophisticated instrumentation [2]. Addressing these obstacles requires not only technological innovation but also a thorough comprehension of the fundamental principles of techniques in observational astronomy.

The experiments conducted in this spectroscopy report serve as a starting point to introduce some of the foundational methods and tools of astronomical observation. The report focuses on four experiments: Grating Spectrograph, Solar Spectrum, Prism Spectrometer, and Spectrography, all of which provide a hands-on approach to understanding the principles of spectral analysis, a technique that underpins modern astrophysics research.

Each experiment offers insights into the methods used to study different aspects of the

universe. For instance, spectral analysis is critical for determining chemical compositions, temperatures, and physical conditions of the celestial bodies scientists are attempting to research [3]. This is specifically employed in the spectrograph experiment, where the emission lines of various elements are analysed to identify them.

In linking these experiments to real-life cases, it becomes evident that the techniques learned here are the building blocks for addressing larger scientific questions. They build an understanding of how simple localised observations in an undergraduate laboratory can contribute to constructing models of the universe. By establishing a strong foundation in these fundamental methods, these experiments provide a starting point for future research and exploration in astronomy.

All *Python* scripts and data can be found [here](#).

II. GRATING SPECTROGRAPH

A. Background

A spectrograph is used to separate light from a source into its constituent wavelengths to produce a spectrum. It does this by passing the incoming light through a small slit in a metal plate to isolate light from a single area or object

which is bounced off a diffraction grating, which then disperses the light into its wavelengths [4].

It is comprised of four main components. The slit isolates light from a specific source and determines the spectral resolution, with narrower slits improving resolution by reducing overlap of spectral lines but with lower light intensity. The collimator ensures the light exiting the slit is collimated (i.e. made parallel), which is crucial for accurate interaction with the disperser. The disperser, typically a diffraction grating, separates light into its constituent wavelengths. The groove spacing of the grating determines the degree of dispersion and resolution, with finer spacings offering higher spectral resolution by more effectively separating closely spaced wavelengths. Different gratings, characterized by varying groove densities, produce spectra with differing levels of detail and intensity. Finally, the camera focuses the dispersed light onto the detector, forming the image of the spectrum for observation and analysis.

There are two types of diffraction gratings; Reflective and Transmission. This experiment uses a reflection grating, which is a surface with finely spaced grooves that disperse the incoming wave into its wavelengths [5]. In the context of the experiment, this allowed the visible light to be broken down into its constituent colours. This is a common technique employed in astronomy to study the chemical compositions of celestial objects. For example, it can help identify the atmospheric makeup of an exoplanet to determine whether or not it is habitable.

When light encounters a grating, it is diffracted at specific angles depending on its wavelength. The relationship between the two can be derived simply by considering the geometry presented below in fig. 1.

The total path difference Δ is characterised by the sum of Δ_1 and Δ_2 which can be found through trigonometry:

$$\begin{aligned}\Delta_1 &= d \sin \theta, \\ \Delta_2 &= d \sin \varphi, \\ \Delta &= d(\sin \theta + \sin \varphi).\end{aligned}$$

For the two beams to constructively interfere

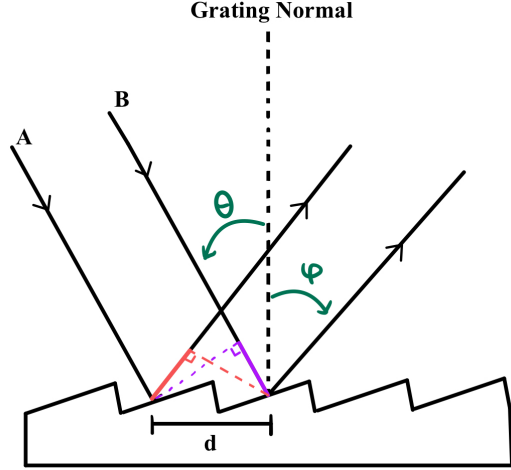


FIG. 1: The incident light beams, A and B, strike the grating grooves at an angle θ to the normal separated by the groove spacing d . The diffracted beams emerge at an angle φ and are separated by the spacing d . The extra distance that B travels compared to A is the path difference, *Delta*. The purple highlighted length is the path difference before reflection, Δ_1 , and the red highlighted length is the path difference after reflection, Δ_2 .

and form bright spectral lines that are visible, the total path difference must be an integer multiple of the wavelength, λ , to lead to maxima:

$$\Delta = m\lambda.$$

Equating this to the total path difference above, we find the familiar grating equation:

$$m\lambda = d(\sin \theta + \sin \varphi), \quad (1)$$

where d is the groove spacing, θ is the incident angle of the ray relative to the grating normal, φ is the reflected (or diffracted) angle relative to the grating normal, m is the diffraction order, and λ is the wavelength of light.

B. Method

This experiment aimed to investigate the functionality of a grating spectrograph by examining the influence of its components on the resulting spectra. The report primarily focused on the effects of varying the slit width and grating configuration. These adjustments facilitated the identification of an optimal setup that maximized the resolution of the output spectra, making it suitable for precise measurements. The primary objective was to determine the groove spacing of two different reflection gratings using the wavelengths of the visible spectrum produced by white light.

The experimental setup was aligned such that the angle of incidence, θ , was set to zero, and measurements were restricted to the first-order ($m = 1$) maxima. Under these conditions, the grating equation was simplified to:

$$\sin \varphi = \frac{\lambda}{d}, \quad (2)$$

where d is the groove spacing, λ is the wavelength of light, and φ is the angle of reflection. Simplifying the equation in this way reduced the complexity of data collection, as only the reflection angle φ needed to be measured to calculate the groove spacing. Once θ was aligned, the experimental setup formed a right triangle, allowing for straightforward measurements, as shown in fig. 2.

A range of y was measured for corresponding colours in the visible spectrum, with each measurement repeated three times to improve precision. Further repetitions were not possible due to time constraints. y was measured to the middle of each colour as the spectrum is continuous and a consistent point needed to be chosen. The distance x was measured once, after which the slit position and width were kept constant. Both x and y were measured using a standard meter stick.

Using basic trigonometry φ can be calculated for each y using the following relation:

$$\varphi = \arctan \frac{y}{x}, \quad (3)$$

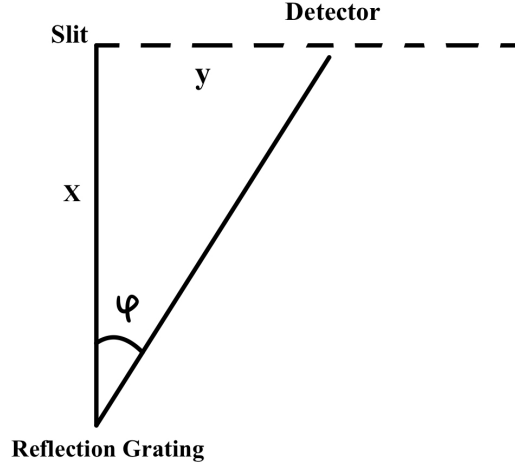


FIG. 2: Diagram of the experimental setup illustrating the right triangle formed. Here, x represents the distance from the slit to the reflection grating, and y is the distance from the slit to the first-order spectrum.

Substituting these values into eq. (2), d was calculated for each corresponding wavelength λ . Since the groove spacing is a physical property of the grating, it was expected to remain constant for all measurements.

Additionally, the groove spacing of the second grating was estimated by comparing it to the measured spacing of the first grating. This was achieved using the ratio of the sine of the reflection angles for the two gratings:

$$d_2 = d_1 \frac{\sin \varphi_1}{\sin \varphi_2}, \quad (4)$$

where the subscripts denote the corresponding grating. This approach allowed the comparison between the measured and expected values for the second grating's groove spacing.

In order to find d_1 and d_2 , eq. (2) must be fit with a linear model where y is $\sin \varphi$, x is λ , and d is the gradient of the straight line to be plotted. This also implies a zero y-intercept on the graph.

C. Uncertainties

Uncertainties associated with λ , y , φ , and d are discussed in this section. The wavelengths λ were sourced from an online reference [6], which provided a range of values for each colour. The midpoint of the range was taken as the value of λ , while the uncertainty, $\delta\lambda$, was calculated using the half-range rule:

$$\delta\lambda = \frac{|a - b|}{2}, \quad (5)$$

where a and b are the minimum and maximum values of the range, respectively. This approach implicitly assumes a symmetric distribution of values around the midpoint and assumed Gaussian errors.

The uncertainties in the remaining variables required a more systematic approach. For functions of multiple variables, $f(x_1, x_2, \dots, x_n)$, the general analytical propagation of uncertainty is given by:

$$\delta f = \sqrt{\sum_{i=1}^n \left(\frac{\partial f}{\partial x_i} \delta x_i \right)^2}, \quad (6)$$

where δx_i represents the uncertainty in each independent variable [7].

For measurements taken in multiple trials, the uncertainty was estimated using the standard deviation, σ , and the error on the mean, $\sigma_{\bar{x}}$. These calculations, introduced in the *Fourier Analysis and Statistics* course, are shown in eq. (7) and eq. (8):

$$\sigma = \sqrt{\frac{1}{N} \sum_{i=1}^N (x_i - \mu)^2}, \quad (7)$$

$$\sigma_{\bar{x}} = \frac{\sigma}{\sqrt{N}}, \quad (8)$$

where x_i are the individual measurements, μ is their mean, and N is the number of trials.

For the error propagation of y , both its measurement uncertainty, δ_{meas} , (from measuring the distance with a ruler) and a calculation of the error on its mean using eq. (8) have to be combined. This was done using a root sum squared as follows:

$$\delta_{tot} = \sqrt{\delta_{meas}^2 + \sigma_{\bar{x}}^2}. \quad (9)$$

where the measurement uncertainty was estimated by accounting for parallax error during measurements and the determination of the distance to a continuous colour spectrum. These errors are expected to be random and symmetric around the expected value, again implying a Gaussian error.

Required uncertainties can then be calculated by applying eq. (6) to eq. (3), eq. (4), and $\sin \varphi$ as follows:

$$\delta\varphi = \sqrt{\left(\frac{\delta y \cdot x}{y^2 + x^2} \right)^2 + \left(\frac{\delta x \cdot y}{y^2 + x^2} \right)^2},$$

$$\delta(\sin \varphi) = \delta\varphi \cos \varphi, \quad (10)$$

$$\delta d_2 = \sqrt{\left(\frac{\sin \varphi_1}{\sin \varphi_2} \delta d_1 \right)^2 + \left(d_1 \frac{\cos \varphi_1}{\sin \varphi_2} \delta \varphi_1 \right)^2 + \left(d_1 \frac{\sin \varphi_1 \cos \varphi_2}{\sin^2 \varphi_2} \delta \varphi_2 \right)^2} \quad (11)$$

To complement the analytical error propagation, a Monte Carlo simulation was performed as introduced in *Numerical Recipes* [8]. Random samples of λ and φ were drawn from normal distributions centred at their respective means, with standard deviations corresponding to their uncertainties. As all errors so far had been assumed to be Gaussian the same was done here. For each sample, a linear model was fitted to calculate d . The mean and standard deviation of the resulting distribution of d values provided its estimate and uncertainty. Finally,

it should be noted that due to the random sampling inherent in a Monte Carlo simulation, each run generates slightly different results, making it a non-deterministic process. This was not considered as the differences were deemed negligible.

D. Results

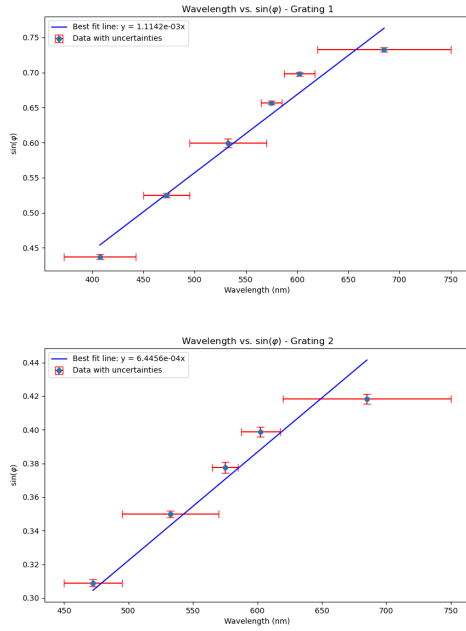


FIG. 3: Linear fits of $\sin(\varphi)$ vs. λ for Gratings 1 and 2. The inverse of the slopes of the fitted lines correspond to the groove spacings, d_1 and d_2 , respectively. The data follows a strong linear trend as expected for both gratings. The respective analytical uncertainty calculations were done as presented in the previous section leading to error bars presented.

Graphs were plotted to investigate the relationship between $\sin \varphi$ and corresponding λ , shown in fig. 3. A least-squares fit was applied to determine the groove spacing, d . The regression was performed using `scipy.optimize.curve_fit`, which pro-

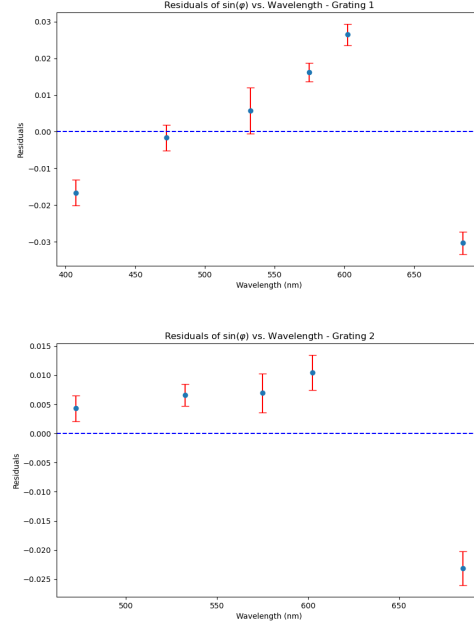


FIG. 4: A residuals plot using the uncertainty of $\sin \varphi$ is also presented for both gratings. These were calculated as the difference between the observed $\sin \varphi$ and the values predicted by the linear regression for both gratings and used to assess the quality of fit.

vides both the best-fit parameters and a covariance matrix. The diagonal elements of the covariance matrix represent the variances of the fitted parameters, and their square roots give the standard deviations, which were taken as the uncertainties in the gradients of the best-fit lines, and are presented following:

$$d_1 = 900(12) \text{ nm}, \quad d_2 = 1550(26) \text{ nm} \quad (12)$$

Next, using eq. (4), eq. (11) and values from eq. (12), d_2 was also determined as a function of d_1 . The value of $\sin \varphi$ could be chosen at any wavelength, provided it was consistent across both gratings. The blue wavelength was selected here, resulting in:

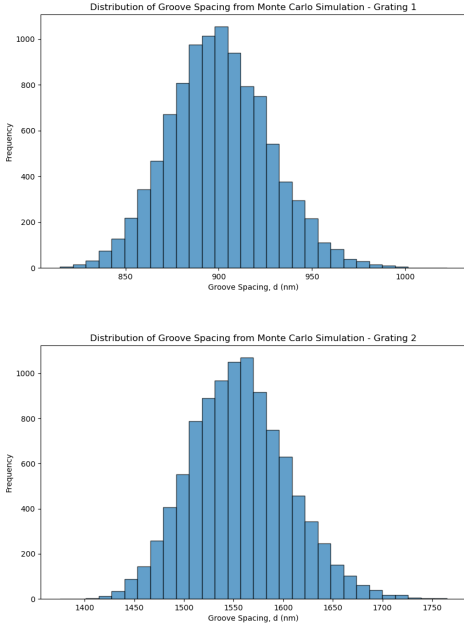


FIG. 5: This figure represents the normally distributed values sampled for the groove spacing by the Monte-Carlo Simulation. It is centred at d_i with a standard deviation δd_i . It visualises the variability in d_i showing its probabilistic nature.

$$d_2 = 1520(21) \text{ nm}, \quad (13)$$

which is in agreement with the measured value in eq. (12).

Finally, the values determined using the Monte-Carlo Simulation are presented with respective uncertainties. Alongside, a visualisation of the distribution of the normally sampled groove spacing:

$$d_1 = 900(30) \text{ nm}, \quad d_2 = 1560(50) \text{ nm}. \quad (14)$$

E. Discussion

The model was initially fitted with and without a y -intercept. Including the y -intercept yielded an uncertainty exceeding its value and close to zero, highlighting its insignificance. Hence, a model without a y -intercept was used.

For both gratings, the best-fit line passes through most data points and their error bars, indicating a strong linear relationship between $\sin \varphi$ and λ . However, the wavelength uncertainties, especially in the red region, are substantial due to its large range.

For grating 1, two out of five residuals cross the x -axis, while for grating 2, none do. This suggests underestimated measurement uncertainties and unexpected errors rather than a failure of the linear regression. Residuals for grating 1 are semi-randomly spread, but grating 2 shows deviation above the x -axis, indicating systematic errors, possibly from faint spectral lines or set-up misalignment. Coefficients of determination, $r^2 = 0.96$ for grating 1 and $r^2 = 0.90$ for grating 2, confirm strong linear fits, with grating 1 having a better fit.

Monte Carlo uncertainties (eq. (14)) are roughly double those from analytical propagation, reflecting its ability to account for input variability, whereas analytical propagation may underestimate true uncertainty.

Systematic errors could arise from deviations in the assumed zero incidence angle θ or surface damage on the gratings. Random errors likely stemmed from inconsistent y measurements, as the chosen points for measurement varied subjectively.

The results aligns with theory that closer-spaced gratings offer higher spectral resolution, evident from clearer spectra for grating 1. Further exemplified by grating 2's lower r^2 and its lack of detectable violet lines, lower resolution, and greater difficulty in data collection.

Future improvements could include more precise θ alignment, automated y measurement, increasing data points, and repeating measurements under varied conditions to reduce uncertainties and better identify error sources.

III. SOLAR SPECTRUM

A. Background

Fraunhofer lines are dark absorption features observed in the solar spectrum. These lines originate from the absorption of specific wavelengths of sunlight by atoms in the cooler outer layers of the solar atmosphere [9]. Each element absorbs light at characteristic wavelengths, making these lines a valuable tool for identifying the Sun's chemical composition. For example, the presence of calcium, sodium, and hydrogen can be inferred from prominent Fraunhofer lines such as the H and K lines of the Calcium II doublet in the violet part of the spectrum or the D_1 , D_2 sodium doublet [10].

In addition to solar atmospheric absorption, Earth's atmosphere introduces absorption features known as telluric lines [11]. These are caused by water vapour and oxygen present in the Earth's atmosphere. Telluric lines vary significantly depending on local atmospheric conditions, such as humidity and elevation, which makes them an important consideration for ground based observations.

When measurements are taken with the Sun directly overhead (at zenith), the light passes through a minimal amount of Earth's atmosphere, reducing the influence of Telluric lines. The amount of atmosphere the sunlight passes through is known as airmass and refers to the effective column of the atmosphere through which it passes [11]. In contrast, when the Sun is observed closer to the horizon, the light travels a much longer atmospheric path (higher air mass), increasing the absorption effects of water vapour, oxygen, and other atmospheric molecules. This phenomenon directly affects the intensity and depth of Telluric lines in the observed spectrum.

B. Method

Due to cloudy weather, original measurements could not be taken, and backup data was

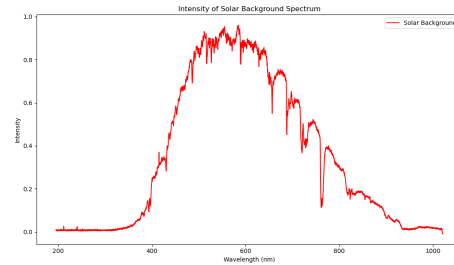


FIG. 6: This is a background spectra of the atmosphere by simply pointing the fibre optic cable up, an integration time of 450ms was found to produce reasonable spectra. This is representative of a typical solar spectrum expected.

used instead. However, the intended method is described below.

This experiment involves measuring the solar spectrum and comparing absorption features observed at different elevations. A CCD spectrograph, attached to a mini telescope of focal length 25mm via an optical fibre input was employed to capture the solar spectrum. Three neutral density (ND) filters were used to prevent over saturation by absorbing light uniformly across all wavelengths. Different elevations were also considered when capturing spectra due to absorption and scatter effects mentioned earlier.

While the setup differs from a traditional spectrograph, the same principles of light dispersion discussed above are applicable. The resulting spectra allow for the identification of key absorption lines caused by elements in the solar atmosphere and Earth's atmosphere. In this case the detector was the ThorLabs software and all data was directly read from it as a plot of relative intensity against wavelength.

C. Results

The angular size of the Sun on the optical fibre cable was estimated to be approximately 1mm by inspection. The result was verified by

using the basic optics equation for small θ in radians,

$$x = f\theta = 0.2218\text{mm}$$

where x is the size of the image and f is the telescope focal length. For $\theta = 0.5^\circ$ the diameter of the solar image was found to be smaller than estimated.

The Sun completes a full rotation (360°) around the Earth in 24 hours. Therefore, the time taken for the Sun to move its angular diameter (0.5°) is calculated as:

$$\text{Time} = \frac{24 \times 60 \text{ mins}}{360^\circ} \times 0.5^\circ = 2 \text{ mins.}$$

The expected value provided by the TA's was ≈ 10 mins. Potential reasons for the discrepancies in the size of the image and time are due to the lens being deliberately defocused by the manufacturer to increase the effective size of the image on the focal plane to improve its resolution.

The Fraunhofer and Telluric lines were identified and over-plotted on the solar spectrum found with the ND1 filter. The filter was chosen as it had the highest intensity amongst all three filters and provided a strong signal-to-noise ratio when compared to fig. 6 which allowed easy identification of the absorption lines.

A normalised solar spectra for different elevations ($45^\circ, 90^\circ$, and the horizon) is also presented.

D. Discussion

Inspection of fig. 8 reveals slight discrepancies between the measured and expected wavelengths of the Calcium doublet, though these fall within the ThorLabs spectrograph's resolution uncertainty ($\delta = 0.3 \text{ nm}$) [9]. These differences likely stem from the instrument's resolution limits, calibration errors, or measurement uncertainties, though this is difficult to confirm as it represents backup data.

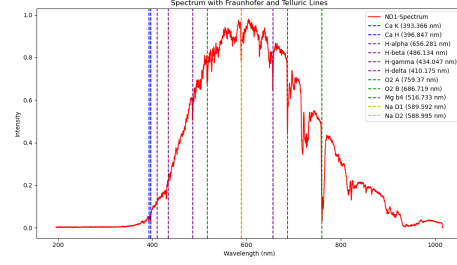


FIG. 7: Filtered solar spectrum highlighting the detected absorption lines. The Oxygen and Magnesium telluric lines are shown in green with other prominent Fraunhofer lines labelled appropriately. The dotted lines are plotted using theoretical values and align well with the ones found on the spectra itself [12].

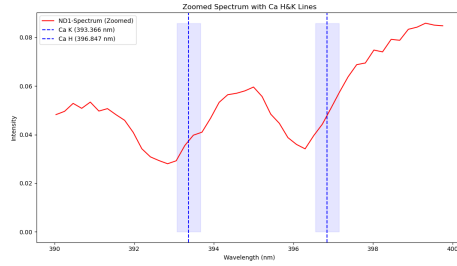


FIG. 8: This is a zoomed in image of the spectra at the Ca K & H lines to identify the doublet. The wavelengths at the centre of each line were identified as 393.270 nm and 396.941 nm and the dotted blue lines represent the expected values of the doublet at 393.366 nm and 396.847 nm, respectively.

In fig. 9 the spectrum at Zenith appears least intense because it has been normalised to 720 nm. When normalized, the spectrum at the horizon is scaled up more significantly, leading to higher relative intensities across the rest of the spectrum. In contrast, the zenith, with minimal atmospheric effects, has a higher original intensity at 720 nm and therefore requires less scaling, making its normalised spectrum appear less intense overall.

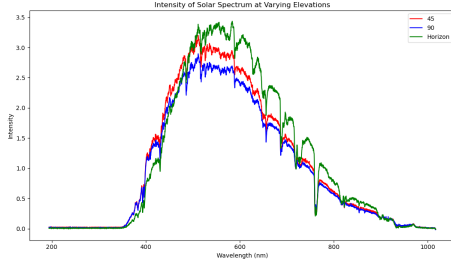


FIG. 9: Solar spectra that has been normalised to 720nm. This was done because there is minimal scattering and absorption near this wavelength since red light will scatter less than blue. This allows an overall comparison of solar spectrum intensity.

Solar spectrum variations can arise from solar activity, such as sunspots and flares, which affect the intensity of Fraunhofer lines associated with elements in active regions [13]. Comparing spectra over time can reveal these variations, offering insights into solar dynamics.

The Tenerife graphs from the lab manual [9] highlight the impact of latitude on solar elevation. In Edinburgh (56°), the maximum solar elevation at summer solstice is approximately 57.5° , whereas in Tenerife (28°), it reaches 85.5° [9, 11]. This means the Sun in Edinburgh is never directly overhead, even at its highest point, while in Tenerife, it comes much closer to the zenith. Consequently, sunlight reaching Edinburgh passes through more airmass, increasing absorption effects compared to Tenerife, where observations are less affected.

The Ca H&K lines, intrinsic to the Sun, are unaffected by Earth's atmosphere, whereas the telluric oxygen A-band lines arise from atmospheric interaction. The A-band features deepen at lower elevations due to increased air mass, confirming their atmospheric origin, while the stability of the Ca H&K lines reflects their solar origin [10].

IV. PRISM SPECTROMETER

A. Background

A prism spectrometer is an alternative type of diffraction grating, which is discussed earlier. Unlike the linear relationship between diffraction angle and wavelength observed in grating spectrographs, prism spectrographs exhibit a non-linear dispersion. In a prism, shorter wavelengths (blue light) deviate more strongly than longer wavelengths (red light), which arises from the dependence of wavelength on refractive index [11].

When light passes through a prism, it is refracted at both the entry and exit surfaces. The total deviation angle, D , is defined as the angle between the direction of the incoming ray and the outgoing ray after passing through the prism. As the angle of incidence, θ_i , is varied, the deviation angle first decreases to a minimum value, D_{min} , before increasing again. This phenomenon is called the angle of minimum deviation, and it occurs when the light traverses the prism symmetrically, i.e., when the angle of incidence equals the angle of emergence, θ_e .

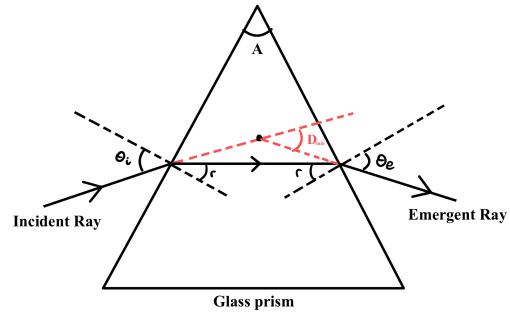


FIG. 10: This diagram showcases when the angle of deviation is at a minimum, occurring when the refracted ray travels parallel to the base of the prism. The relevant angles are: A is the prism angle, r represents the angles of refraction at the prism surfaces, and D_{min} is the minimum angle of deviation.

A relation between the prism angle, A , the

refractive index, n , and the minimum deviation angle, D_{min} can be derived by using Snell's Law [14]:

$$n_1 \sin(\theta_i) = n_2 \sin(\theta_e), \quad (15)$$

where n_1 and n_2 are the refractive indices of the two media, θ_i is the angle of incidence, and θ_e is the angle of emergence. For the prism, $n_1 \approx 1$ (in air), and $n_2 = n$, the refractive index of the prism material.

Considering eq. (15) at the prism's surface and substituting $\theta_i = \theta_e$ as we are only interested in the minimum deviation. The prism angle, A , is related to the angle of refraction, r , by symmetry as:

$$A = 2r.$$

The total deviation angle, D_{min} , is the angle between the initial incident ray and the final emergent ray. At minimum deviation, it is given by:

$$D_{min} = 2\theta_i - A.$$

Rearranging the above gives:

$$\theta_i = \frac{D_{min} + A}{2}.$$

Substituting θ_i into eq. (15) and using the relation for A , the refractive index n of the prism material is given by [15]:

$$n = \frac{\sin\left(\frac{D_{min} + A}{2}\right)}{\sin\left(\frac{A}{2}\right)}. \quad (16)$$

Furthermore, n is not a material constant but depends on colour and varies as a function of wavelength λ . This variation can be described by a power series that was empirically determined and known as the Cauchy dispersion relation:

$$n(\lambda) = C_1 + \frac{C_2}{\lambda^2} + \frac{C_3}{\lambda^4} + \dots,$$

where C_1 , C_2 , and C_3 are constants determined empirically, and λ is the wavelength of light [16]. For narrow spectral ranges, higher-order terms can often be neglected, simplifying the equation to:

$$n(\lambda) \approx C_1 + \frac{C_2}{\lambda^2}. \quad (17)$$

Due to the narrow range of λ being considered here eq. (17) is expected to behave linearly with C_1 dominating over the short range, hence, C_1 will represent a value for n once fitted. Linearising eq. (17) yields:

$$n\lambda^2 = \lambda^2 C_1 + C_2, \quad (18)$$

which can be applied to make a linear model as before with the grating spectrograph.

B. Method

This experiment aimed to measure the refractive index, n , of a prism as a function of wavelength using a prism spectrometer. A helium lamp served as the light source, positioned approximately 1 cm in front of the spectrometer slit. The collimator was aligned to produce a parallel beam of light, the telescope was positioned 180° from the collimator, and was adjusted for height and focus such that the image in the slit was centred on the crosshairs.

The dispersed colour spectrum produced by the prism was found and the prism table and telescope were adjusted until a 'bounce back' of the moving spectra was noticed—this represented the point of D_{min} as the angle started shifting. At this point the crosshair was used to measure the angle for multiple spectral lines emitted by the lamp. Five measurements were taken for D_{min} for each wavelength in order to mitigate random error. The straight through

angle was also added onto each D_{min} which was measured when the non-refracted light from the lamp through the slit was incident on the centre of the telescope. The refractive index, n , for each wavelength was calculated using eq. (16) where $A = 60^\circ$ since the prism was equilateral.

Two models were then fit to the data using eq. (18) and eq. (17) by using `scipy.optimize.curve_fit`. Comparisons between the fits were made to assess their accuracy and applicability.

C. Uncertainties

Uncertainties were propagated for λ , D_{min} , and n using the same wavelengths and uncertainties as outlined in section II C. To compute δn , eq. (6) was applied to eq. (16), yielding:

$$\delta n = \frac{\delta D_{min} \cos\left(\frac{D_{min} + A}{2}\right)}{2 \sin\left(\frac{A}{2}\right)}. \quad (19)$$

The uncertainty in D_{min} , δD_{min} , was calculated by combining its standard deviation, derived using eq. (7) and eq. (8), with its measurement uncertainty estimated as $\delta D_{min, meas} = 0.0003$ radians. This value was based on parallax, instrumental errors during observations and the error introduced by the straight through angle—their combination was performed using eq. (9).

As the Monte-Carlo error simulation was successful with the grating spectrograph it was applied here to propagate uncertainties in D_{min} and calculate the refractive index n . Since n depends solely on D_{min} , as per eq. (16), random samples of D_{min} were generated from a normal distribution centred on the measured mean, with a standard deviation of δD_{min} as calculated earlier. The mean and standard deviation of the resulting n samples provided the estimated value and its uncertainty for each corresponding wavelength.

D. Results

The following table is presented in addition to the equation in fig. 11, with analytical uncertainties calculated as detailed above and n found through eq. (16).

Wavelength (nm)	Refractive Index
410(40)	1.53(3)
470(20)	1.52(2)
530(40)	1.521(10)
580(10)	1.516(11)
670(70)	1.514(12)

TABLE I: This table presents the refractive indices and their associated uncertainties for five distinct wavelengths of light to highlight n 's dependence on λ .

The relationship between refractive index and wavelength was plotted, as shown in fig. 11. Both the linear regression and Cauchy model fits were over-plotted on the experimental data for comparison. The residuals of these fits are presented in fig. 12.

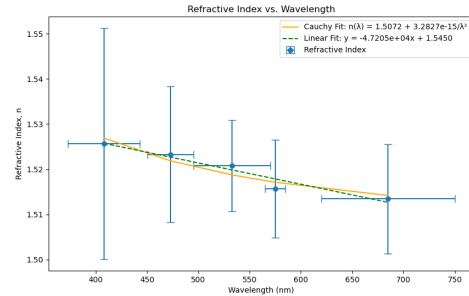


FIG. 11: Measured refractive index as a function of wavelength. The plot includes experimental data with error bars, a linear regression fit, and a fit based on the Cauchy dispersion relation, highlighting the dependence of n on λ . The C_1 constant term for the Cauchy fit is a general value of the refractive index and C_2 is its correction term.

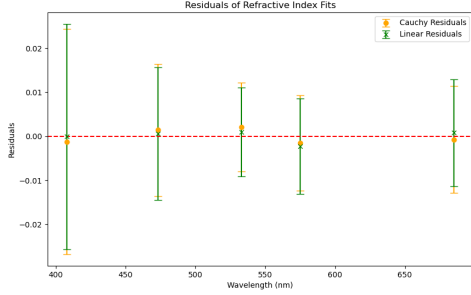


FIG. 12: Residuals of the linear and Cauchy fits to the refractive index data.

Wavelength (nm)	Refractive Index
410(40)	1.53(3)
470(20)	1.523(15)
530(40)	1.521(10)
580(10)	1.516(11)
670(70)	1.513(12)

TABLE II: Refractive Indices determined using a Monte-Carlo Simulation. It is noticed that the values determined and their respective uncertainties are very similar to the analytical approach, unlike the grating spectrograph.

E. Discussion

As shown in fig. 11, n shows a nearly linear relationship with λ , reflecting limited dispersive variation in the prism over the narrow range. This causes the constant C_1 term in the Cauchy equation to dominate. The slight decrease in n with increasing λ is consistent with eq. (17) and the background discussion, supporting the linear model.

The fits in fig. 11 show that both linear and Cauchy models approximate n well. Residuals in fig. 12 are randomly distributed around zero, indicating no significant bias. The refractive index values in table I and table II are nearly identical, confirming that analytical error propagation provided reasonable estimates.

Although both models perform similarly, the linear model is simpler and more practical for

the narrow wavelength range, with a slightly higher r^2 (0.94) than the Cauchy model (0.90). The Cauchy model, however, remains useful for understanding non-linear dispersion, especially for broader wavelength ranges or materials with higher dispersion.

Uncertainties in n , shown by error bars in fig. 11 and fig. 12, consistently cross the x-axis in the residuals plot, suggesting overestimated uncertainty in D_{min} . Ideally, about 2/3 of points should cross the x-axis, as per the expected normal distribution of uncertainties [17]. The overestimation likely results from conservative instrumental error estimates or redundant sources.

This overestimation affects the Monte Carlo simulation as δD_{min} influences the sampling process in the simulation. However, the residuals are sufficiently close to zero that even smaller uncertainties would not significantly alter this conclusion.

The random residuals close to zero indicate minimal systematic errors. Minor biases could arise from setup misalignments, such as imprecise prism positioning or collimator alignment, though these do not materially affect conclusions. Improving alignment and calibration would enhance D_{min} consistency and error insight.

Improvements in the alignment and calibration of the prism spectrometer could reduce uncertainties in D_{min} as well. For example, a more precise mechanism for setting the prism at the exact angle of minimum deviation could enhance consistency across measurements.

V. SPECTRAL LAMPS AND COLOUR FILTERS

A. Background

The background needed for this experiment has been covered in section II A and section III A. The same spectrometer was used as in the solar spectrum experiment and it generates a spectrum using a diffraction grating.

Colour filters are tools used to isolate specific ranges of wavelength and measure their flux. A transmission curve, found as the ratio between transmitted and incident light intensity, describes how efficiently a filter transmits flux at different wavelengths. Colour filters are used for photometry to measure the brightness of stars in specific wavelength bands, identify spectral features, and determine physical properties to facilitate studies of stellar and galactic properties. They also aid in distinguishing between different types of astronomical objects by emphasising specific emission or absorption features.

For example, as presented by Gaustad et al. (2001) using a narrowband filter centred around the H-alpha line (656.3 nm) can help isolate the flux originating from hydrogen transitions in stars or nebulae. Similarly, filters targeting the oxygen [O III] line (500.7 nm) are essential for studying planetary nebulae or star-forming regions [18].

B. Method

There were two aims in this experiment. The first was to identify the constituent elements of different gas lamps by analysing the spectra produced by the light's dispersion through comparison to literature values. The second was to generate transmission curves for combinations of colour filters and discuss interesting cases.

The spectrometer was calibrated using a helium lamp, by mapping its pixel output to known wavelengths from the lab manual [9]. This ensured that subsequent measurements of unknown spectra or filter transmission curves were reliable and could be compared to standard laboratory values. Background light was minimised by turning off external light sources and corrected for by recording a background trace with the light source turned off to subtract away.

This calibration was then applied and spectra were taken for a range of different unknown lamps on ThorLabs. Individual background correction was applied with respective integra-

tion times in each case with careful consideration of longer integration times leading to higher errors. Emission spectra were identified by using the NIST ASD Database^[19] and its *Search for Lines* tool, with a tolerance used around the peak wavelengths for each spectra based on the resolution uncertainty in the ThorLabs spectrograph to identify corresponding peaks for different elements.

Given that gas discharge lamps were used, when trying to identify them focus was placed on noble gases and additional common materials such as hydrogen, mercury, and sodium [20]. For each spectral peak, only the two to three most relatively intense elements were considered, as the remaining contributions were too weak to be significant. The element that appeared most consistently across 4–5 prominent peaks and exhibited the highest intensity was identified as the most likely candidate.

For the colour filters the Helium filament lamp was fitted back as the light source. The unfiltered spectrum of the bulb was recorded and saved as a reference trace after adjusting the integration time to avoid saturation. Transmission curves were then calculated by dividing the curve with the colour filter by the white light trace of the lamp.

C. Uncertainties

An uncertainty was determined in the calibrated wavelengths by comparing the measured and expected values of the peaks of the Helium filament lamp. Expected values were presented in the lab manual and measured values were from the Helium spectra found on ThorLabs. A root-mean-square deviation was used to estimate the error as it quantifies the average discrepancy between measured and expected values, effectively capturing the spread of the calibration errors.

$$\text{RMSD} = \sqrt{\frac{1}{N} \sum_{i=1}^N (\lambda_i - \lambda_{\text{ref},i})^2} \quad (20)$$

N is the number of data points, λ_i is the observed wavelength, and $\lambda_{\text{ref},i}$ is the reference wavelength.

This resulted in a value of $RMSE = 0.11$ nm, which was combined with the resolution uncertainty provided in the ThorLabs Software manual using eq. (9), giving $\delta\lambda = 0.3$ nm. Which was then used as the applied tolerance for the peaks evaluated to identify the spectral lamps in order to maintain conservative estimates.

D. Results

The spectra of the Helium lamp and all eight unknown lamps with their identified element are presented below.

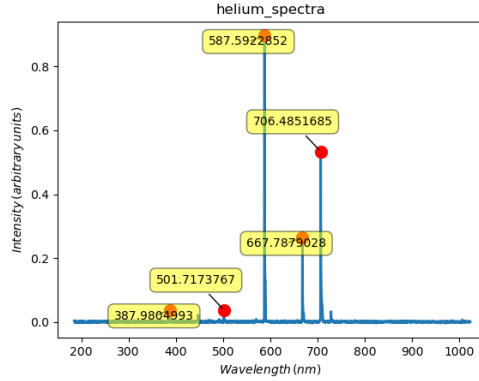


FIG. 13: Emission spectra of the Helium lamp taken after calibration was completed with integration time 3.8s. This ensured that consequent spectra had accurate pixel to wavelength calibrations.

The colour filter transmission curves are presented below. For reference, FW1-1 indicates filter wheel 1 and colour 1, while FW2-1 denotes filter wheel 2, colour 1. In all graphs, the black curve (Spectrum 1) represents the white light trace, the blue curve (Spectrum 2) shows the filtered trace, and the green curve (Spectrum 3) corresponds to the transmission curve.

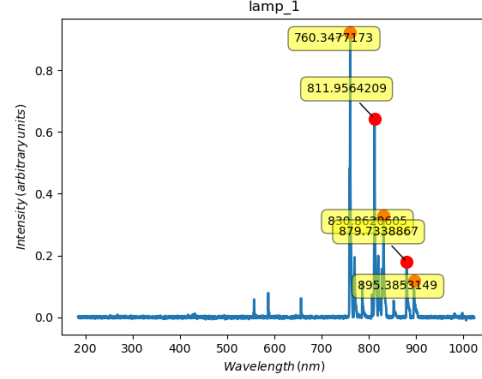


FIG. 14: Spectra for lamp 1 taken with integration time 15s. It was confidently identified as **Krypton** due to its intense peaks near 760 and 811 nm.

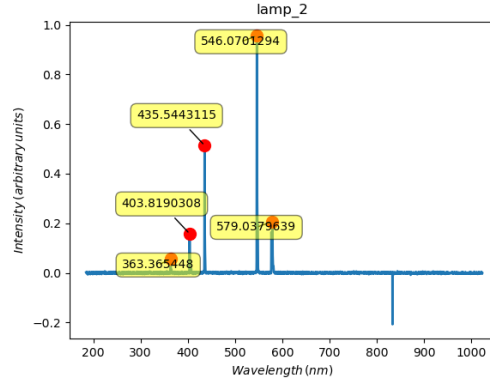


FIG. 15: Spectra for lamp 2 taken with integration time 8s. It was confidently identified as **Mercury** due to the two intense peaks at 546 and 435 nm.

The erratic behaviour observed at the beginning of each graph is due to a division-by-zero error caused by the white light trace being zero for the lower wavelengths, leading to irregularities in the calculated transmission. A consistent integration time of 425ms was used across all measurements to minimise the influence of background light and quick data collection.

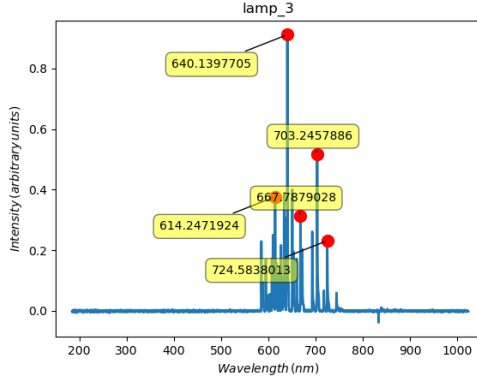


FIG. 16: Spectra for lamp 3 taken with integration time 1.5s. It was confidently identified as **Neon** due to the peaks near 640 and 703 nm.

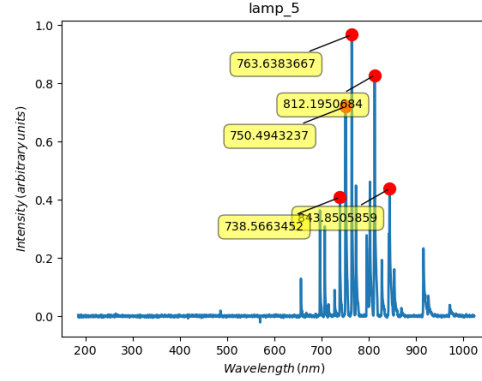


FIG. 18: Spectra for lamp 5 taken with integration time 1.5s. It was confidently identified as **Argon** due to the primary peaks it has near 640 and 703 nm. Traces of lamp 2 were also found with Mercury peaks at 763 and 738 nm.

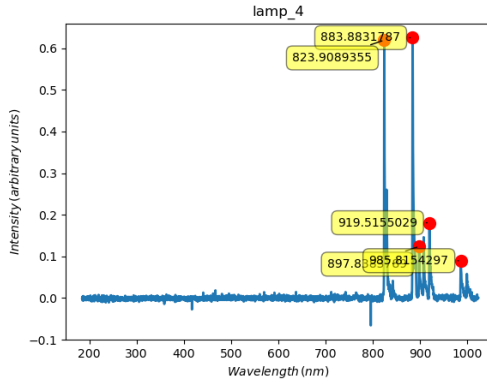


FIG. 17: Spectra for lamp 4 taken with integration time 50s. It was identified as **Xenon** with low confidence after analysis of all 5 peaks.

E. Discussion

A key observation was that longer integration times reduced confidence in element identification. This was because extended periods increased error margins and background interference, as highlighted in the narrow peak at 833 nm in both fig. 19 and fig. 20.

To improve element identification, wavelength tolerance was adjusted. If only one or two elements matched the initial tolerance, the threshold was slightly increased to avoid overlooking borderline elements. For instance, in lamp 1, the initial analysis identified only Argon for one peak, but extending the tolerance revealed Krypton with a higher relative intensity. Furthermore, confidence in element identification could have been further improved by recording the observed colours of the lamps during data collection or photographing the lamps.

Finally, the colour filters are instrumental in isolating specific spectral features by selectively transmitting or blocking light at certain wavelengths. For instance, combining the filters shown in fig. 23 and fig. 25 allows targeting of blue and yellow spectral features while suppressing red components. By isolating key features of a spectrum, filters facilitate focused analysis, enabling the determination of critical information about the spectral source, whether terrestrial or celestial.

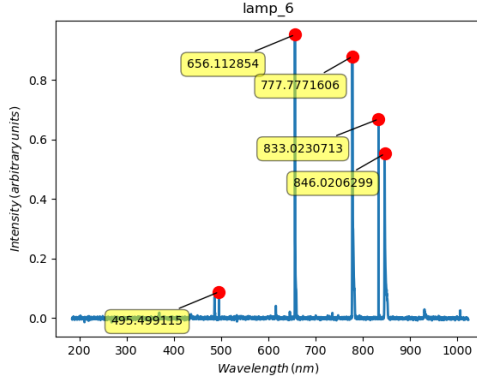


FIG. 19: Spectra for lamp 6 taken with integration time 32s. It was identified as **Oxygen** with low confidence by using its peaks at 777 and 846 nm. The peak at 833 nm was attributed to significant background disturbances and the peak at 656 nm is trace Hydrogen.

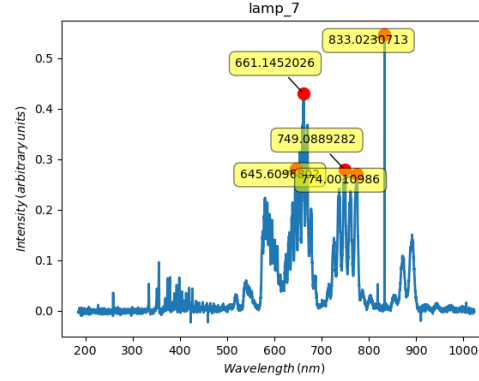


FIG. 20: Spectra for lamp 7 taken with integration time 80s. It was identified as **Nitrogen** with partial confidence because of the peak at 656 nm and the observed broad spectrum which is typical of Nitrogen. The peak at 833 nm due to background disturbances is noticed again and was ignored.

VI. CONCLUSION

The basic principles applied in these experiments are easily extended to study distant stars, galaxies, and nebulae. By analysing absorption and emission lines, inferences can be made of specific elements, map interstellar gas clouds, and even detect exoplanetary atmospheric structures. The use of prisms and grating spectrographs to disperse light into constituent wavelengths allows for detailed spectral analysis, not only locally, but of distant stars and planets as well. Analysis of the wavelength of light from celestial objects also enables our understanding of the dynamics of distant systems through Doppler shifts, uncovering phenomena like galaxy rotation, and the expansion of the universe [11].

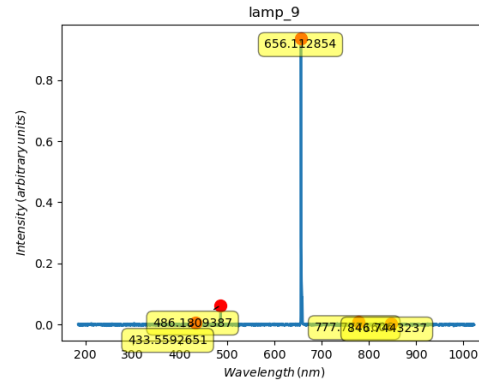


FIG. 21: Spectra for lamp 9 with integration time 2.2s. Only the primary peak at 656 nm was needed to identify this lamp confidently as **Hydrogen** since its relative intensity is very high.

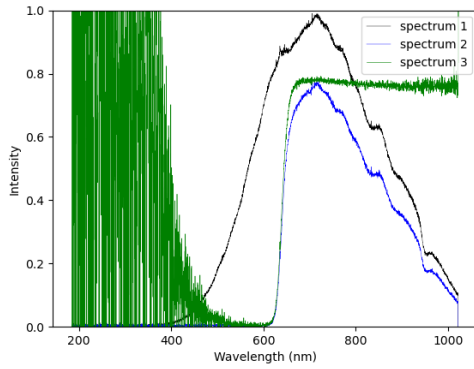


FIG. 22: This is a single filter transmission curve using FW1-2. This filter appears to completely block light below 600 nm while allowing light above that to pass through. This is indicative of a long-pass filter which filters wavelengths smaller than a cut off value [21].

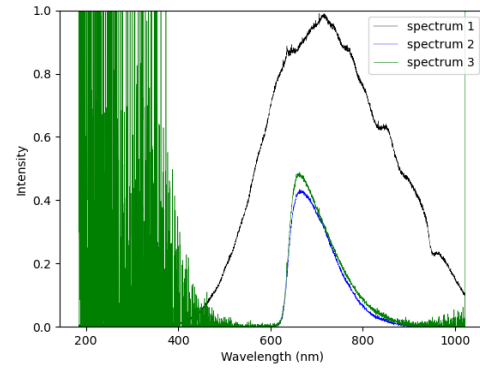


FIG. 24: This is a two filter combination transmission curve using FW1-2 and FW2-3. This combination appears to transmit light in the red to near-infrared range (approximately 650–800 nm) while blocking shorter wavelengths below ≈ 600 nm. The peak suggests this is also a bandpass filter designed to isolate red wavelengths.

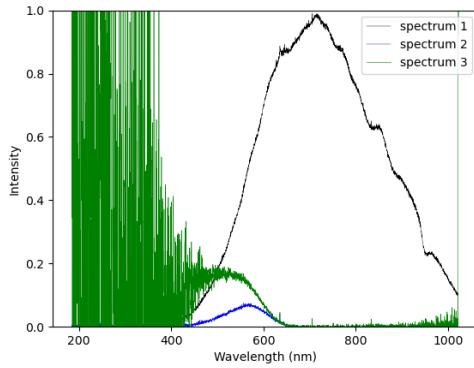


FIG. 23: This is a single filter transmission curve using FW1-3. This filter seems to be a bandpass filter as it blocks light only in the 450 - 650 nm range [22]. It has a sharp peak here with fast declines either side of it suggesting it will be useful for analysing spectra with blue features.

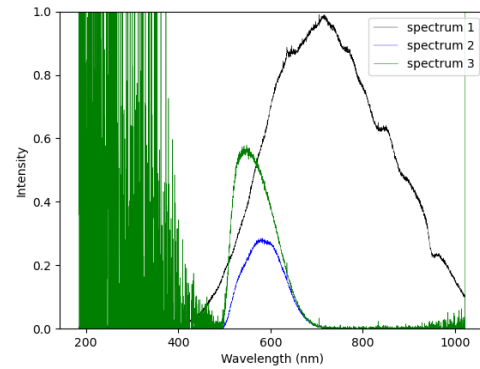


FIG. 25: This is another bandpass filter as it only allows wavelength in the wavelength range of approximately 500 nm - 700 with a peak near 600 nm. It blocks majority of red and blue light allowing primarily yellow and green light through.

-
- [1] G. Jogesh Babu and S. George Djorgovski. Some statistical and computational challenges, and opportunities in astronomy. *Statistical Science*, 19(2):322–332, 2004.
- [2] E. D. Feigelson and G. J. Babu. Statistical challenges in modern astronomy, 2004.
- [3] Jonathan Tennyson. *Astronomical Spectroscopy: An introduction to the Atomic and Molecular Physics of Astronomical Spectra*. Imperial College Press, 2nd edition, 2005.
- [4] NASA. spectroscopy: Reading the rainbow, 2022. [Accessed 20-11-2024].
- [5] Definition of reflection grating. [Accessed 20-11-2024].
- [6] Anne Marie Helmenstine. The visible spectrum: Wavelengths and colors, 2024. [Accessed 21-11-2024].
- [7] James L. Gardner. Uncertainties in spectral color measurement, 2007. [Accessed 20-11-2024].
- [8] Britton Smith and Sergey Koposov. *Lecture 6: Random Number Algorithms*. The University of Edinburgh, 2024. Slides 31 - 41.
- [9] Sadegh Khochfar and Ross McLure. *Junior Honours Astrophysics Lab Handbook*. learn page for ‘observational astronomy’, 2024.
- [10] David F. Gray. *The Observation and Analysis of Stellar Photospheres*. Cambridge University Press, 3 edition, 2005.
- [11] Ross McLure. *obs astro 2024 semester1 combined notes*. learn page for ‘observational astronomy’, 2024.
- [12] Francis A. Jenkins and Harvey E. White. *Fundamentals of Optics*. McGraw-Hill Science Engineering, 4th edition, 1976. Appendix V: THE MOST INTENSE FRAUNHOFER LINES.
- [13] A. I. Shapiro, S. K. Solanki, N. A. Krivova, R. V. Tagirov, and W. K. Schmutz. The role of the Fraunhofer lines in solar brightness variability. , 581:A116, September 2015.
- [14] David Halliday, Jearl Walker, and Robert Resnick. *Principles of Physics: International student version*. John Wiley and Sons, Inc., 9 edition, 2010.
- [15] Max Born and Emil Wolf. *Principles of Optics: Electromagnetic Theory of Propagation, Interference and Diffraction of Light*. Cambridge University Press, 7th edition, 1999. Section on dispersion, covering Cauchy’s formula.
- [16] Eugene Hecht. *Optics*. Pearson Education, 5th edition, 2017. Chapter 5, discussion of prisms and minimum deviation.
- [17] Malcolm McMahon. *The Object of Experimental Physics*. The University of Edinburgh, version 2.32 edition, 2023.
- [18] John E. Gaustad, Peter R. McCullough, Wayne Rosing, and Dave Van Buren. A Robotic Wide-Angle H α Survey of the Southern Sky. , 113(789):1326–1348, November 2001.
- [19] A. Kramida, Yu. Ralchenko, J. Reader, and NIST ASD Team. NIST Atomic Spectra Database (ver. 5.12), [Online]. Available: <https://physics.nist.gov/asd> [2024, November 25]. National Institute of Standards and Technology, Gaithersburg, MD., 2024.
- [20] Asim Kumar Roy Choudhury. Characteristics of light sources. In Asim Kumar Roy Choudhury, editor, *Principles of Colour and Appearance Measurement*, pages 1–52. Woodhead Publishing, 2014.
- [21] Iridian Spectral Technologies. The basics of long pass filters. https://www.iridian.ca/learning_center/light-notes/basics-long-pass-filters/?srsltid=AfmB0orwOG2cPRcxcR2Ewj2YFKTdMXfJ1D6Bu5xG81VXUNUle7y43ch. [Accessed 27-11-2024].
- [22] Envin Scientific. What are band-pass filters and why are they important? <https://www.envinsci.co.uk/what-are-optical-bandpass-filters/#:~:text=Optical%20bandpass%20filters%20are%20filters,to%20a%20very%20wide%20range.>, 2024. [Accessed 27-11-2024].
- [23] OpenAI ChatGPT. Chat transcript on spectrography lab report formatting, November 2024. AI-generated assistance for LaTeX document preparation and citation creation. Also conservatively used to improve clarity of writing by improving conciseness.